



Tin dioxide nanomaterial-based photocatalysts for nitrogen oxide oxidation: a review

Viet Van Pham^{*1}, Hong-Huy Tran¹, Thao Kim Truong¹ and Thi Minh Cao²

Review

Open Access

Address:

¹Photocatalysis Research Group (PRG), Faculty of Materials Science and Technology, University of Science, VNU–HCM, 227 Nguyen Van Cu Street, District 5, Ho Chi Minh City, 700000, Viet Nam and
²HUTECH University, 475A Dien Bien Phu Street, Binh Thanh District, Ho Chi Minh City, 700000, Viet Nam

Email:

Viet Van Pham^{*} - pvviet@hcmus.edu.vn

^{*} Corresponding author

Keywords:

green products; nanomaterials; NO oxidation; photocatalysis; SnO₂

Beilstein J. Nanotechnol. **2022**, *13*, 96–113.

<https://doi.org/10.3762/bjnano.13.7>

Received: 07 October 2021

Accepted: 30 December 2021

Published: 21 January 2022

This article is part of the thematic issue "Nanomaterials for photocatalysis and applications in environmental remediation and renewable energy".

Associate Editor: C. T. Yavuz

© 2022 Van Pham et al.; licensee Beilstein-Institut.

License and terms: see end of document.

Abstract

Semiconducting SnO₂ photocatalyst nanomaterials are extensively used in energy and environmental research because of their outstanding physical and chemical properties. In recent years, nitrogen oxide (NO_x) pollutants have received particular attention from the scientific community. The photocatalytic NO_x oxidation will be an important contribution to mitigate climate change in the future. Existing review papers mainly focus on applying SnO₂ materials for photocatalytic oxidation of pollutants in the water, while studies on the decomposition of gas pollutants are still being developed. In addition, previous studies have shown that the photocatalytic activity regarding NO_x decomposition of SnO₂ and other materials depends on many factors, such as physical structure and band energies, surface and defect states, and morphology. Recent studies have been focused on the modification of properties of SnO₂ to increase the photocatalytic efficiency of SnO₂, including bandgap engineering, defect regulation, surface engineering, heterojunction construction, and using co-catalysts, which will be thoroughly highlighted in this review.

Review

Introduction

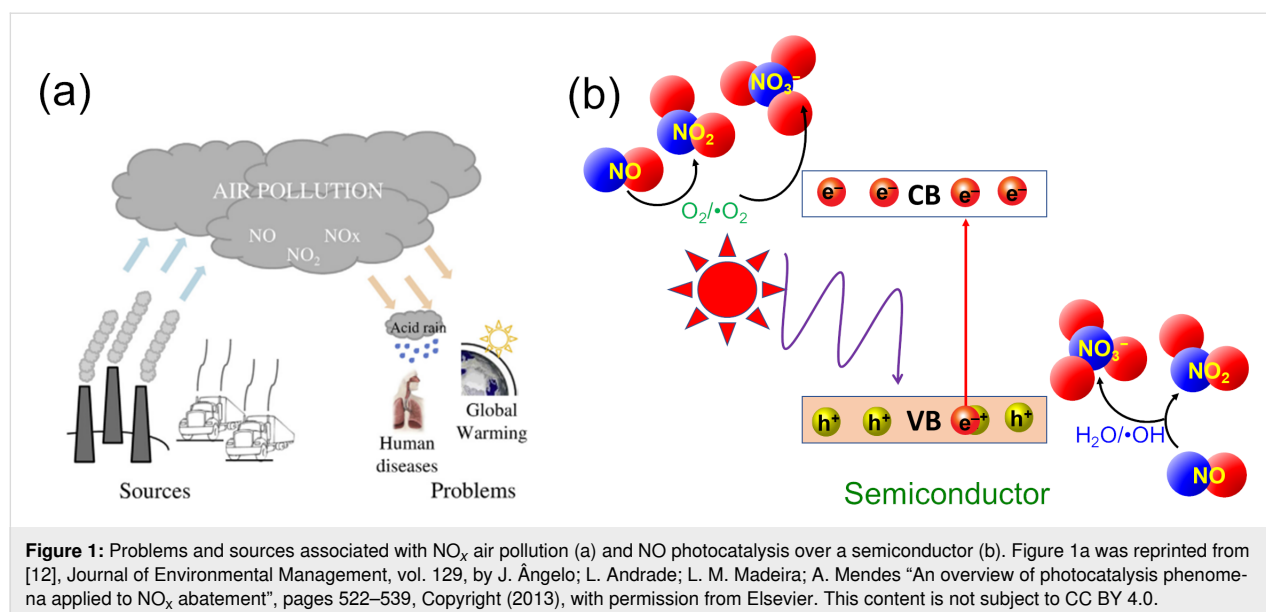
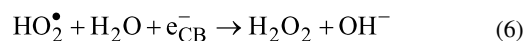
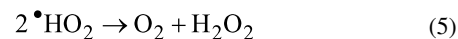
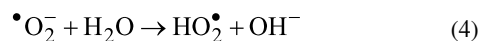
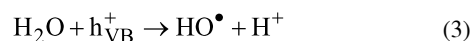
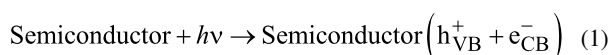
A World Health Organization (WHO) report indicated that 4.2 million deaths every year occur due to exposure to ambient (outdoor) air pollution [1]. This number is much higher than the deaths from the COVID-19 pandemic in the past year. WHO also reported that the emissions of nitrogen oxides in the early 1980s over the world were estimated at approximately

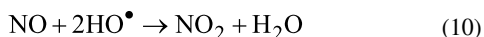
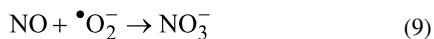
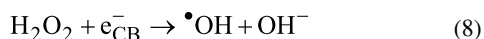
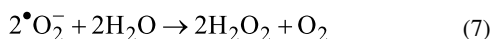
150×10^{12} g/year while the concentration of nitrogen dioxide outdoor can achieve up to 940 µg/m³ (0.5 ppm) for 30 min and 400 µg/m³ (0.21 ppm) for 60 min [2]. Nitrogen oxides (NO_x, including NO and NO₂) are poisonous and highly reactive gases. Nitrogen dioxide (NO₂) is associated with respiratory diseases and mortality. NO_x is formed when fuel is burnt at high temper-

atures and emitted by automobiles, trucks, and various non-road vehicles (e.g., construction equipment, boats) and industrial sources such as power plants, industrial boilers, cement kilns, and turbines [3]. In addition, diesel vehicles are considered a primary NO_x emission source causing adversely impacts on environment and human health, such as acid rain, global warming, and respiratory diseases in humans (Figure 1a). NO_x pollution damages lung cells and reacts with molecules in the air when released into the ozone layer. NO_x can aggravate respiratory diseases such as asthma, bronchitis, and cardiovascular diseases. When humans are exposed to NO_2 at concentrations of over $200 \mu\text{g}/\text{m}^3$, even for periods of time, this will cause adverse effects on the respiratory system. Some studies have shown that NO_2 concentrations over $500 \mu\text{g}/\text{m}^3$ can cause acute health effects. Although the lowest threshold for NO_2 exposure with a direct effect on lung function in asthmatic subjects was $560 \mu\text{g}/\text{m}^3$, NO_2 exposure to concentrations over $200 \mu\text{g}/\text{m}^3$ caused pulmonary responses in asthmatic people [4,5]. Guillaume P. Chossière et al. indicated that reducing NO_x in the air will significantly reduce the risk of death in humans demonstrated through a study on lockdowns during the COVID-19 pandemic in China that led to a reduction of NO_2 , O_3 , and $\text{PM}_{2.5}$ concentrations globally, resulting in ca. 32,000 avoided premature mortalities, including ca. 21,000 in China [6]. Therefore, the control, treatment, and conversion of NO_x to green products greatly interested the scientific community in recent years.

There are many methods for controlling and removing NO_x , such as reducing the burning temperature, reducing the residence time at peak temperature, chemical reduction or oxidation of NO_x , removal of nitrogen from combustion fuels, and

sorption, both adsorption and absorption [7,8]. Among them, photocatalytic oxidation is an efficient method of converting NO_x into nitrate (NO_3^-) ions. The removal of NO_3^- ions is easy, efficient, and economic through chemical or biological methods such as the conversion of NO_3^- to N_2 by aerobic microorganisms [9,10]. Figure 1b illustrates the working scheme of semiconductor photocatalysts for NO oxidation. Light generates holes (h^+) in the valence band (VB) and electrons (e^-) in the conduction band (CB) of the photocatalytic material. Electrons at the material surface will react with oxygen molecules to form superoxide radicals ($\cdot\text{O}_2^-$, similarly holes react with water to form hydroxyl radicals). Free radicals and strong oxidizing agents react with NO_x to produce NO_3^- , deposited on the photocatalyst surface. The NO_3^- product formed on the surface of the catalyst can be easily separated for further treatment by washing with water due [11] (see Equations 1–10).





Recently, research on tin dioxide (SnO_2) materials has increased significantly, which expresses the potential of SnO_2 materials for the scientific community (Figure 2a). SnO_2 is one of the most extensively investigated n-type semiconductors. It is known as tin(VI) oxide or stannic oxide (not to be confused with stannous oxide with tin in the oxidation state of 2+ [13], also known as cassiterite [14]). SnO_2 materials have many interesting properties. For instance, the structure and electronic structure can be manipulated easily due to the highly tunable valence state and oxygen vacancy defects (OVs) [15,16]. Therefore, SnO_2 is considered a potential material in various technological fields such as catalysis, optoelectronic devices, rechargeable lithium batteries, electrocatalysis, photocatalysis, solar energy conversion, and gas sensing [17–24]. In the catalytic area, SnO_2 is an emerging material for removing contaminants such as organic dyes, phenolic compounds, and volatile organic compounds (VOCs) due to strongly oxidizing properties thanks to flexible energy band structure, rich defects, good chemical, and high thermal stability, and easily controlled morphology [25–30]. However, pure SnO_2 suffers from some inherent drawbacks that limit its practical applications. With a wide bandgap (3.5–3.7 eV) [31,32], SnO_2 can only be excited by UV irradiation. As a typical oxidation photocatalyst with the CB edge energy level, which is not conducive to the reduction of O_2 to $\bullet\text{O}_2^-$ [31,33] and the rapid recombination rate of photoinduced electron–hole pairs [34], the photocatalytic ability of SnO_2 is

less efficient than that of other semiconductor photocatalysts (Figure 2b). Despite literature relating to the unfavorable CB edge of SnO_2 , many reports still proposed its photocatalytic behaviors partly based on $\bullet\text{O}_2^-$ species via the combination of experimental physicochemical analyses, such as electron spin resonance (ESR) spectroscopy, active species trapping experiments, valence band X-ray photoelectron spectroscopy (XPS), and diffuse reflectance spectroscopy (DRS) [35–40]. This promotes a new avenue for diverse analyses of semiconductor photocatalysts in addition to the traditional theories and conclusions.

Previous studies have shown that the photocatalytic activity of NO_x decomposition of materials in general and SnO_2 depends on many factors, including the structure and energy band, surface and defect states, morphology, etc. For that reason, recent studies are being focused on the modification of properties of SnO_2 to upgrade the photocatalytic efficiency of SnO_2 , including bandgap engineering, defect regulation, surface engineering, heterojunction construction, co-catalyst, which will be thoroughly outlined in this review.

Structure and bandgap

SnO_2 has a crystal structure similar to that of rutile TiO_2 [41,42]. The unit cell parameters of rutile SnO_2 are $a = b = 0.47374$ nm and $c = 0.31864$ nm [43]. In one unit cell of rutile SnO_2 , a Sn^{4+} ion is bonded to six oxygen ions, and every oxygen atom is coordinated by three Sn^{4+} ions, forming a (6, 3) coordination structure [44]. When SnO_2 materials are prepared as thin films with two to eight layers the bandgap is larger than that of bulk SnO_2 and decreases with increasing film thickness [45]. Zhou et al. indicated that the direct bandgap transition of SnO_2 has an absorption coefficient α and the optical bandgap (E_g) can be determined by the calculation of

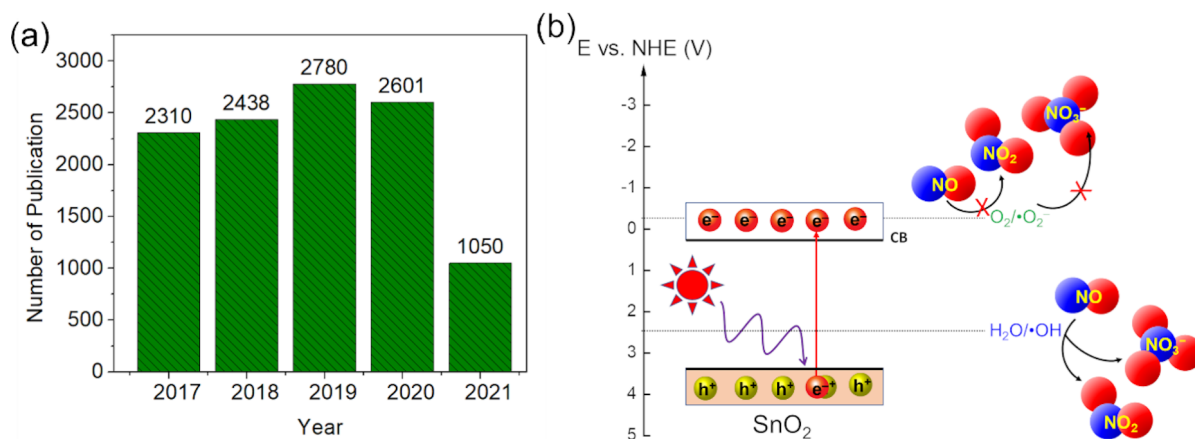


Figure 2: (a) Statistics of publication number on SnO_2 materials (2017–06/2021). Data was extracted from Web of Science, Clarivate Analytics; (b) NO photocatalytic oxidation ability of SnO_2 .

$\alpha(h\nu)^2 \propto (h\nu - E_g)^{1/2}/h\nu$, and the plot of $\alpha(h\nu)^2$ vs photon energy $h\nu$, respectively. For example, the bandgap of a SnO₂ thin film with a thickness of about 130 nm is 3.597 eV [42].

The reported bandgap of bulk SnO₂ is 3.6 eV. Changing the morphology, particle size, or the formation of OV or defects narrow the bandgap. In the study of Babu et al., a redshift of the absorption edge was observed when SnO₂ quantum dots (SQDs) were heated from 200 to 700 °C, which indicated that the bandgap of the SQDs decreased from 3.49 to 2.52 eV (for SQD-700) as shown in Figure 3. These results demonstrated that the redshift is favorable for a photocatalytic activity in the visible light region.

Meanwhile, Fan et al. [47] investigated the bandgap of SnO₂ when changing the self-doping of SnO₂. The change of the color of the powder products and the redshift in the absorption spectra are two quantities that are correlated with each other. Normally, SnO₂ is white and optical absorptions in the visible region arise from changes of the band structure. Moreover, the bandgap of SnO_{2-x} self-doped with Sn²⁺ can be easily determined as follows: A straight line to the x -axis, equaling to the extrapolated value of E_{photon} at $\alpha = 0$, gives the absorption edge energy. This energy parameter corresponds to the bandgap (E_g) of the material [47].

Surface and defect states

Structural defects and lattice imperfections usually bestow most of the properties exploited for applications of SnO₂ materials as they influence various physicochemical properties and reactions on the surface. Most important are defect states of materi-

als, including predominantly point defects, that is, defects associated with one lattice point, such as cation or oxygen ion vacancies. OVs determine the physical and chemical properties of metal oxides. Figure 4a shows the natural crystal structure of SnO₂ synthesized by vapor transport [48]. The (110) plane of rutile SnO₂ is the most common surface, and it is also thermodynamically the most stable [48]. In the rutile phase of SnO₂ in Figure 4b, the (110) plane contains all surface bridging oxygens (1), bridging OVs (2), and oxygen coordinated three- or five-fold (3, 4) with surface tin atoms (Sn 5f). The dual valency of Sn at the surface of SnO₂ plays a role in the reversible transformation of the surface composition from Sn⁴⁺ cations to Sn²⁺, which leads to active centers in the surface chemical process [48]. Moreover, the OVs in SnO₂ often appear when it is synthesized by chemical methods such as sol–gel, hydrothermal, and microwave synthesis [49–51]. The formation and concentration of OVs depend on particle size, synthesizing temperature, and morphology of SnO₂. The OVs play the role of an electron donor and provide free electrons, making SnO₂ an n-type semiconductor [52].

Guoliang Xu et al. indicated that NO could be absorbed easily on various SnO₂(110) surfaces, and it is preferentially adsorbed on the OV site through an N-down orientation. Figure 5 shows the calculation of the energy of NO conversion processes on SnO₂(110), SnO_{2-x}(110), and O₂ + SnO_{2-x}(110) surfaces. The oxidation of NO on other surfaces is determined by the reaction energies, as shown in Figure 5. The O₂ + SnO_{2-x}(110) surface is more exothermic and preferable than other surfaces, which leads to an efficient reaction of NO with the SnO₂ surface [54]. Also, Tiya-Djowe et al. [55] indicated that calcined SnO₂ sam-

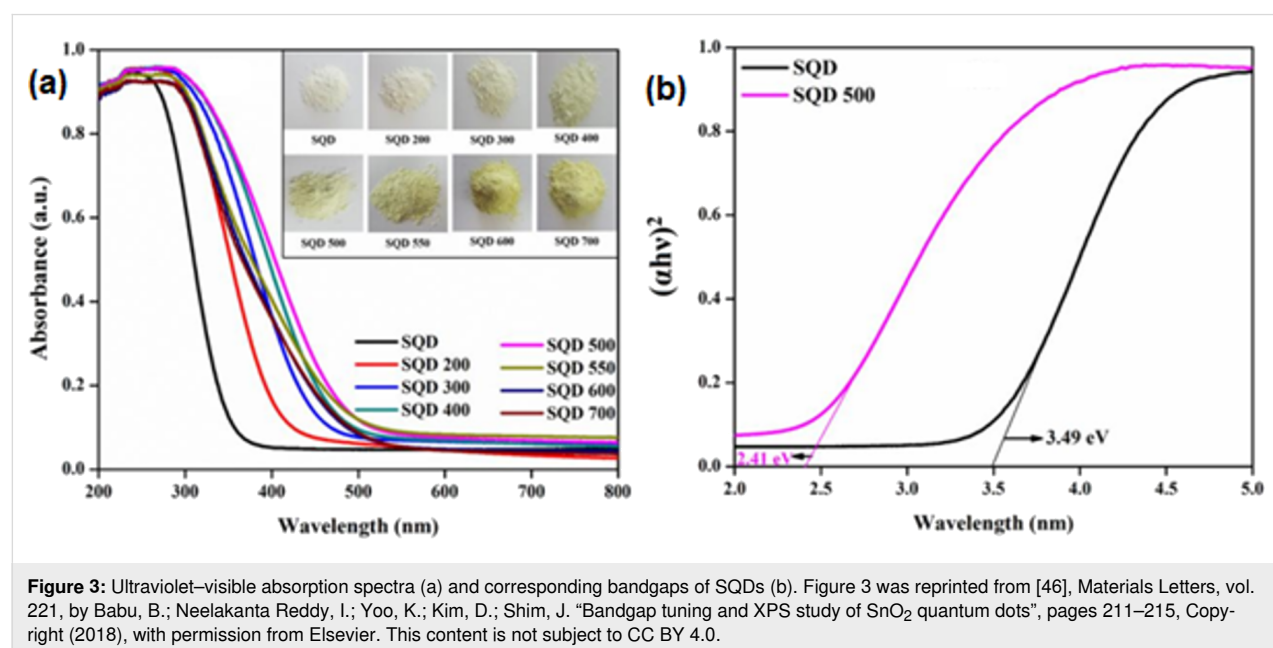


Figure 3: Ultraviolet–visible absorption spectra (a) and corresponding bandgaps of SQDs (b). Figure 3 was reprinted from [46], Materials Letters, vol. 221, by Babu, B.; Neelakanta Reddy, I.; Yoo, K.; Kim, D.; Shim, J. "Bandgap tuning and XPS study of SnO₂ quantum dots", pages 211–215, Copyright (2018), with permission from Elsevier. This content is not subject to CC BY 4.0.

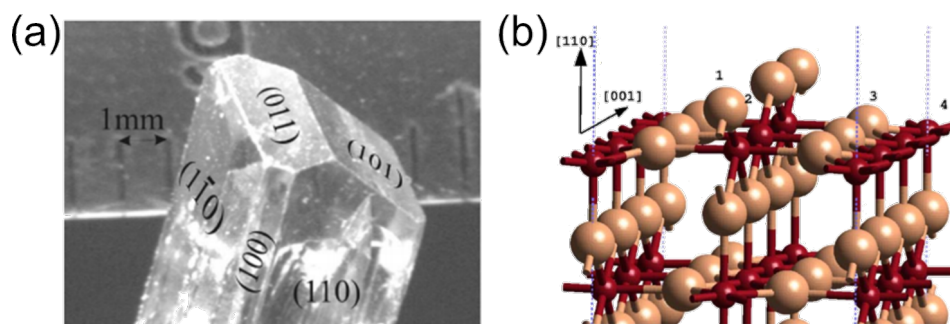


Figure 4: (a) Natural growth faces of SnO_2 are the (110), (100) (equivalent to (010) in rutile), and (101) (equivalent to (011) in rutile) surfaces. Figure 4a was reprinted with permission from [48] (M. Batzill; K. Katsiev; J. M. Burst; U. Diebold; A. M. Chaka; B. Delley, Phys. Rev. B, vol. 72, article no. 165414, 2005). Copyright (2005) by the American Physical Society. This content is not subject to CC BY 4.0; (b) $\text{SnO}_2(110)$ surface including a bridging oxygen vacancy (1-bridging oxygen; 2-bridging OV; 3-oxygen coordinated threefold with surface tin (Sn 5f); 4-oxygen coordinated fivefold with surface tin (Sn 5f)). Figure 4b was reprinted from [53], Surface Science, vol. 577, by Mäki-Jaskari, M. A.; Rantala, T. T.; Golovanov, V. V. "Computational study of charge accumulation at $\text{SnO}_2(110)$ surface", pages 127–138, Copyright (2005), with permission from Elsevier. This content is not subject to CC BY 4.0.

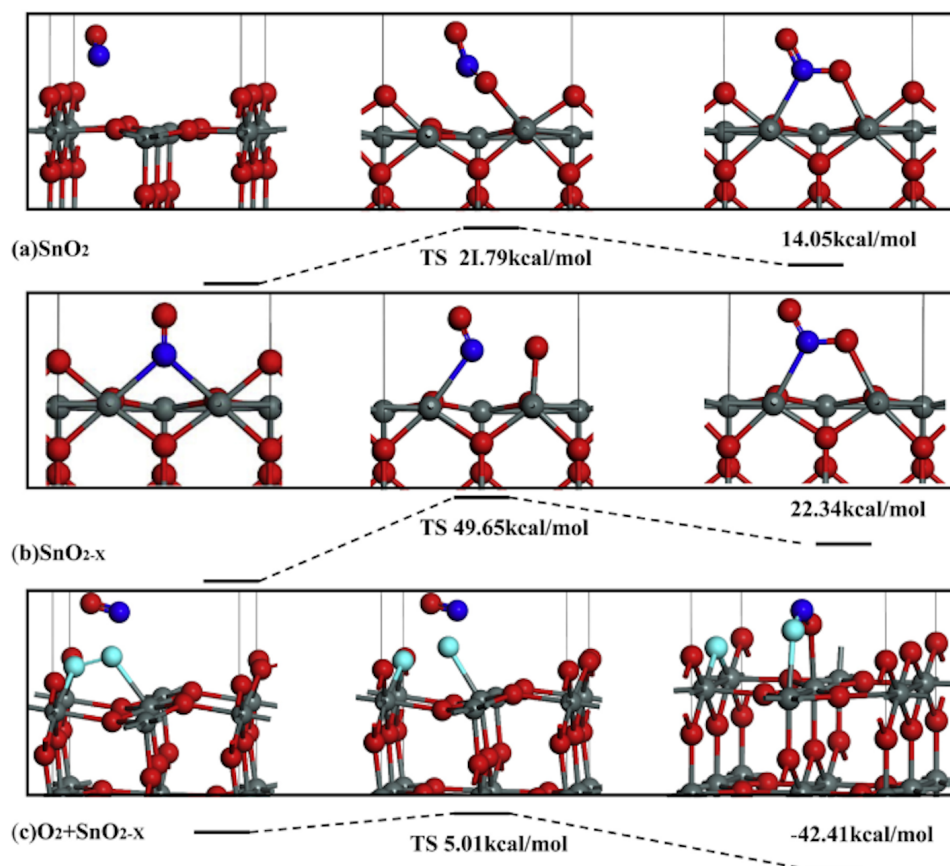


Figure 5: The conversion processes of NO on perfect $\text{SnO}_2(110)$, $\text{SnO}_{2-x}(110)$ and $\text{O}_2 + \text{SnO}_{2-x}(110)$ surfaces. Figure 5 was reprinted from [54], Sensors and Actuators B: Chemical, vol. 221, by Xu, G.; Zhang, L.; He, C.; Ma, D.; Lu, Z. "Adsorption and oxidation of NO on various $\text{SnO}_2(110)$ surfaces: A density functional theory study", pages 717–722, Copyright (2015), with permission from Elsevier. This content is not subject to CC BY 4.0.

ples with higher OV density showed improved photocatalytic performances. Besides, the OV density contributes to the rise of the valence band maximum and a decrease of the bandgap energy of SnO_2 materials.

Morphology

There are many shapes of SnO_2 , for example, nanoparticles, nanocubes, nanorods, nanosheets, nanospheres, nanobelts, and nanotubes. These morphologies can be controllably obtained by

using polyvinylpyrrolidone (PVP), sodium dodecyl sulfonate (SDS), cetyl trimethyl ammonium bromide (CTAB), or tetrapropyl ammonium bromide (TPAB) as surfactants in a hydrothermal method [56–59]. The difference of morphologies will affect the properties of SnO₂ regarding gas sensor activity and optical, electrical, and electrochemical properties [60–63]. The typical properties of SnO₂ are significantly affected by the effective surface area of different nanomaterial morphologies [63–65].

Wang et al. [66] synthesized SnO₂ microspheres on a fluorine-doped tin oxide (FTO) substrate and the SEM images (Figure 6) show SnO₂ microspheres with an average diameter of 2.0–2.5 μm . By using SnO₂ microsphere photocatalysts for the photocatalytic oxidation of NO, Le et al. [67] indicated that 3D hierarchical flower-like SnO₂ microspheres exhibited a photocatalytic activity towards NO decomposition comparable to that of commercial P25 TiO₂. Specifically, SnO₂ microspheres can degrade 57.2% NO (1 ppm of initial concentration) under solar light. However, the photocatalytic mechanism of NO degradation has not been investigated [67]. Zhang et al. [68] found that the crystalline/amorphous stacking structure of SnO₂ microspheres can moderate surface absorption competition between oxygen gas and NO gas, contributing to the generation of reactive oxygen species (ROS) to oxidize NO to NO₃[−] ions. Huy et al. [69] synthesized SnO₂ NPs, and this is the first report on using a SnO₂ photocatalyst with NP morphology for the NO degradation. The photocatalytic mechanism of SnO₂ NPs is based on electrons and holes to generate reactive radicals. Figure 7 shows that the photocatalytic NO removal efficacy of SnO₂ NPs achieved 63.37% after 30 min under solar light irradiation, and the conversion efficacy from NO to NO₂ is 1.66%. The high photocatalytic performance and the stability of SnO₂ NPs under solar light is promising for potential application [69].

Recent approaches in the modification of SnO₂ for photocatalytic NO_x oxidation

Many attempts have been made to enhance the photocatalytic activity and take better advantage of SnO₂ for the NO_x abatement, including the combination with other metal oxides [70], organic semiconductors [71], or metallic nanomaterials [72] to form a heterojunction/composite photocatalyst, and self-doping [73] or elemental doping [39,74]. Hybrid or doped photocatalysts ideally exhibit an improved photocatalytic efficacy due to the reduced recombination rate of photogenerated charge carriers and the lower activation energy. However, additional factors considerably affect the overall photocatalytic process. Table 1 shows a comparison of the NO photocatalytic oxidation ability of neat SnO₂ and modified SnO₂ materials. Recent studies on this material system mainly focus on modifying SnO₂ toward the application in the visible light region.

Charge transfer improvement

The combination of SnO₂ with other co-photocatalysts, including inorganic and organic semiconductors, is a practical approach to enhance the charge transfer efficacy for the photocatalytic process. The photocatalytic degradation of NO_x over SnO₂ as a host photocatalyst is reported to be considerably enhanced after the combination with organic semiconductors such as graphitic carbon nitride (g-C₃N₄) [71]. When acting as an auxiliary photocatalyst, SnO₂ promotes the photocatalytic activity of the primary material [38,70,75,76].

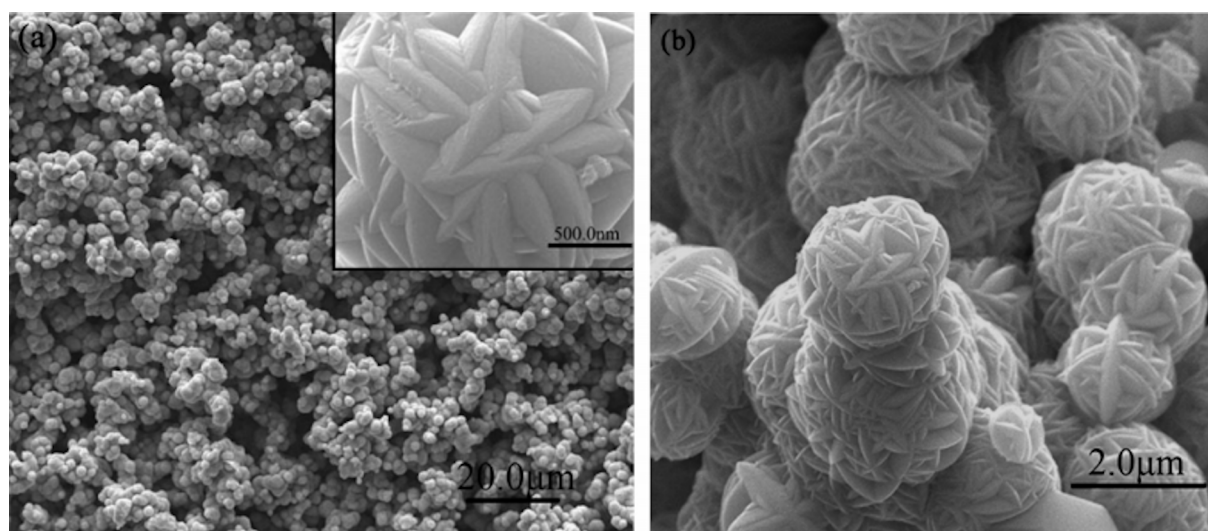
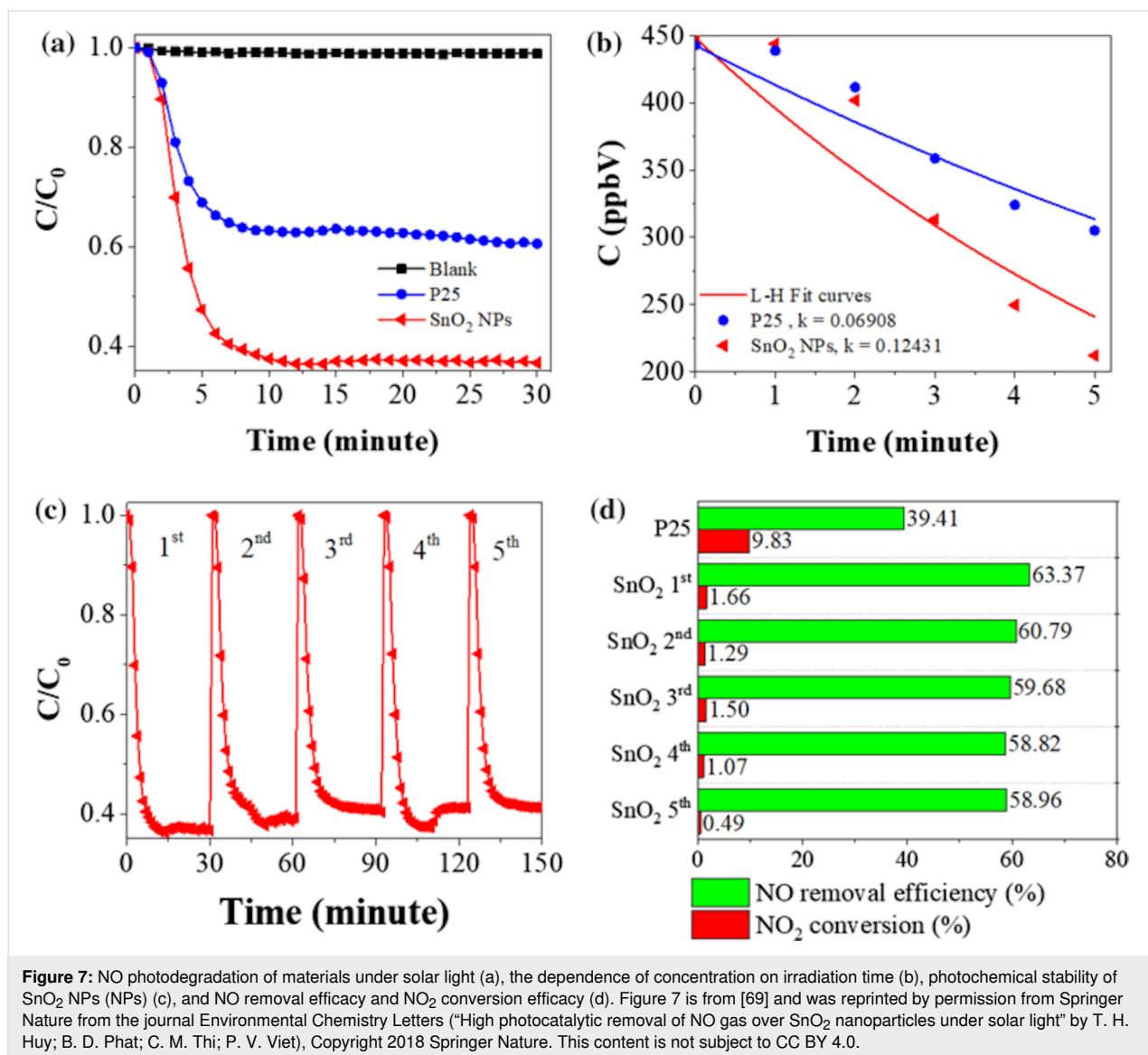


Figure 6: SEM images of SnO₂ microspheres synthesized by a hydrothermal method at 180 °C for 24 h. Figure 6 was reprinted with permission from [66], Copyright 2010 American Chemical Society. This content is not subject to CC BY 4.0.

**Table 1:** A comparison of photocatalytic systems for NO abatement with SnO₂ photocatalyst systems.

Year	Photocatalyst	SnO ₂ morphology	Experimental conditions				NO removal (%)	NO ₂ yield (%)	Ref.
			Light source	Initial NO conc. (ppb)	Humidity (%)	Sample weight (g)			
2013	SnO ₂	microspheres	vis: $\lambda > 510$ nm and $\lambda > 400$ nm; UV: $\lambda > 290$ nm (450 W high-pressure mercury lamp with filters)	10 ³	N/A	N/A	57.2 ($\lambda > 290$ nm) 11.5 ($\lambda > 400$ nm) 4.2 ($\lambda > 510$ nm)	N/A	[67]
2017	SnO ₂ /Zn ₂ SnO ₄ /graphene	unclear shape	vis (3 W LED lamp, $\lambda = 420 \pm 10$ nm)	600	N/A	0.2	59.3	N/A	[75]

Table 1: A comparison of photocatalytic systems for NO abatement with SnO₂ photocatalyst systems. (continued)

2018	SnO ₂	NPs	solar (300 W Xe lamp)	450	70	0.2	63.37	1.66	[69]
2018	SnO ₂ /TiO ₂	NPs	vis (300 W Xe lamp with a UV cutoff filter ($\lambda > 420$ nm))	450	70	0.2	59.49	2.58	[38]
2018	SnO ₂ /graphene	QDs	solar and vis (Xe lamp)	600	N/A	N/A	75 (full spectrum) 57 (vis)	N/A	[36]
2018	SnO ₂ /polyaniline	NPs	solar (300 W Xe lamp)	450	30	0.2	15	8	[35]
2019	SnO ₂ /N-doped carbon quantum dots/ZnSn(OH) ₆	NPs	vis-near-infrared (300 W Xe lamp, $\lambda \geq 420$ nm)	400	30 ± 5	0.2	37	<1.25	[76]
2019	SnO ₂ /g-C ₃ N ₄	QDs	vis (150 W tungsten halogen lamp with a filter ($\lambda > 420$ nm))	600	N/A	0.4	32	8	[37]
2019	Ag@SnO ₂	NPs	solar (300 W Xe lamp)	N/A	N/A	0.2	70	4	[72]
2020	Ce doped SnO ₂	particles	vis (300 W Xe lamp with a UV filter ($\lambda > 420$ nm))	10 ⁴	65	0.4	82	10	[39]
2020	BiOBr/SnO ₂	NPs	vis (150 W tungsten halogen lamp with a UV cut-off filter ($\lambda > 420$ nm))	600	N/A	0.10	50.3	N/A (NO-to-NO ₂ conversion was studied via in situ DRIFTS)	[70]
2021	g-C ₃ N ₄ /SnO ₂	NPs	vis (300 W solar simulator with a UV filter ($\lambda > 420$ nm))	500	70	0.2	44.17	9.29	[71]
2021	SnO _{2-x} /g-C ₃ N ₄	NPs	vis (300 W solar simulator with a UV cut-off filter ($\lambda > 420$ nm))	500	N/A	0.2	40.8	7.5	[73]

Wu et al. reported the visible-light-driven elimination of NO over hydrothermally synthesized BiOBr/SnO₂ p–n heterojunction photocatalysts. The as-prepared BiOBr/SnO₂ photocatalyst with a molar ratio of 2:5 between SnO₂ NPs and BiOBr microspheres shows an enhanced NO_x photocatalytic removal of 50.3%, at an initial NO concentration of 600 ppb, and a great stability after four cycles. The generation of toxic NO₂ products was inhibited effectively. The charge movement at the BiOBr/SnO₂ p–n interface was also revealed via theoretical and experimental findings. Electrons in SnO₂ transfer into BiOBr over pre-formed charge migration channels and an internal electric field at the BiOBr/SnO₂ interface, which directs photoinduced electrons from the CB of BiOBr to that of SnO₂, thus prolonging the lifetime of photogenerated electron–hole pairs (Figure 8). The NO-to-NO₂ conversion and intermediates and products were confirmed via in situ diffuse reflectance infrared Fourier transform spectroscopy during NO oxidation [70].

Huy et al. [38] hydrothermally synthesized SnO₂ NPs adhering to TiO₂ nanotubes (SnO₂/TNTs) via a facile one-step method for the photocatalytic abatement of NO under visible light (Figure 9). At a NO concentration of 450 ppb in a continuous flow, SnO₂/TNTs yields a photocatalytic degradation of NO of 59.49%, which is much better than that of bare TiO₂ NTs (44.61%), SnO₂ NPs (39.55%), and a physical blend of SnO₂ NPs and TiO₂ NTs (39.18%). Also, the heterostructured photocatalyst shows an effective reduction of NO₂ generation after 30 min of photocatalytic reaction. The photogenerated electrons and [•]O₂[−] radicals played a primary role in the photocatalytic NO oxidation. Additionally, using photoluminescence (PL) spectroscopy, XPS, active species trapping tests, and ESR spectroscopy, the authors studied the photoinduced charge migration and trapping. They proposed the band structure of the SnO₂/TNTs and pointed out the existence of [•]O₂[−] and [•]OH radicals as critical factors in the photocatalysis process [38]. These results demonstrated that the SnO₂ NPs could be both a host or an auxiliary material for the NO photocatalytic degradation.

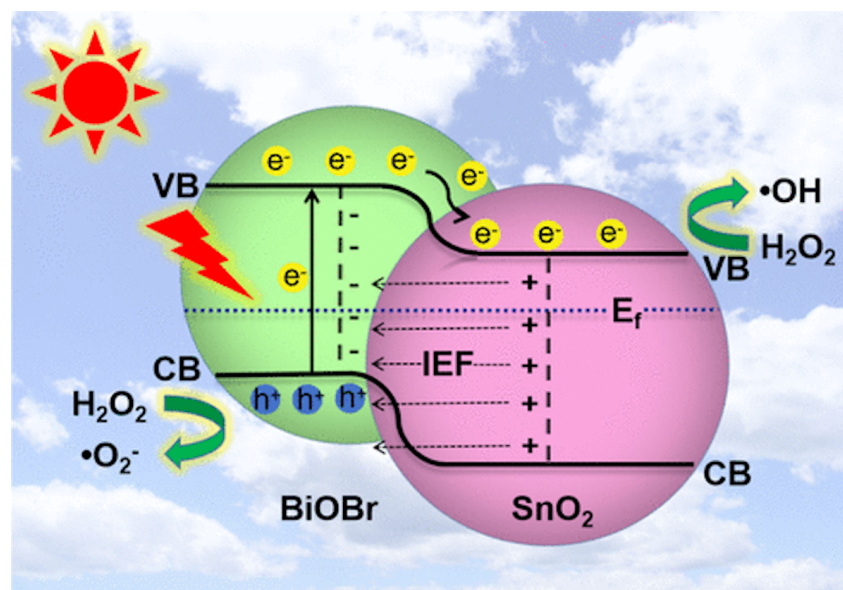


Figure 8: Proposed mechanisms for photocatalytic NO oxidation via interfacial charge migration over BiOBr/SnO₂ p-n heterojunctions. Figure 8 was reprinted with permission from [70], Copyright 2020 American Chemical Society. This content is not subject to CC BY 4.0.

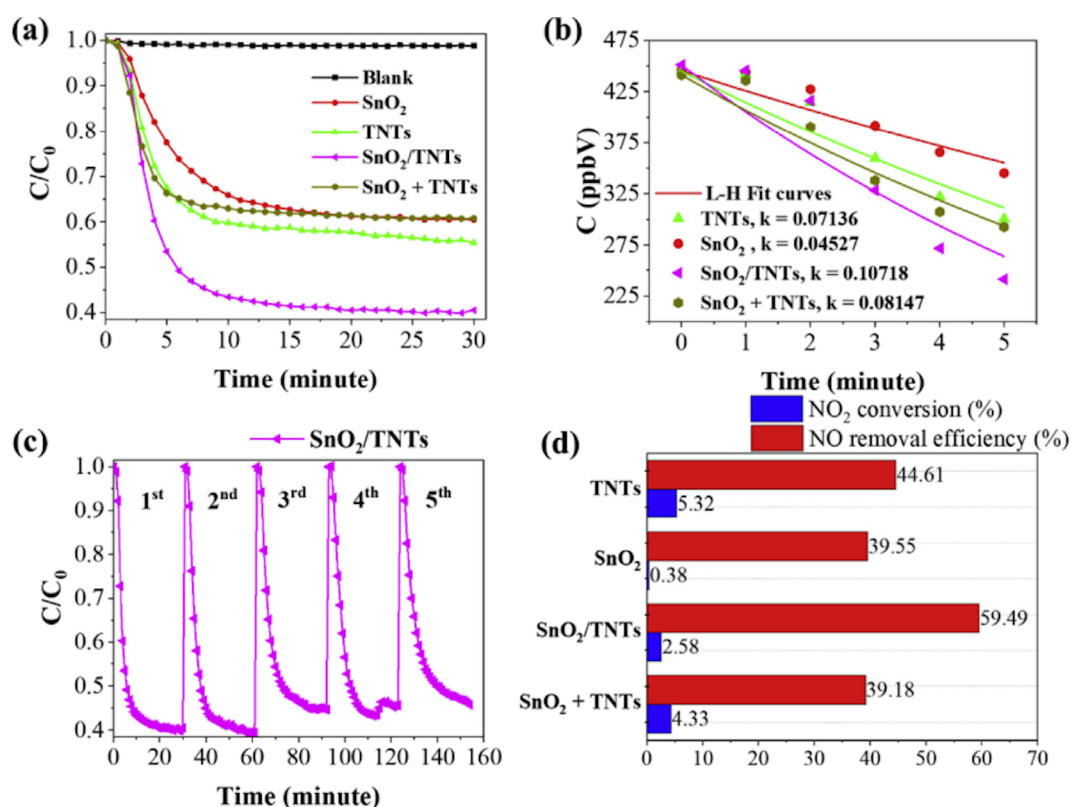


Figure 9: NO photocatalytic degradation of materials under visible light irradiation (a), the dependence of concentration on irradiation time (b), photochemical stability of SnO₂/TNTs (c), and NO removal efficacy and NO₂ conversion efficacy (d). Figure 9 was reprinted from [38], Chemosphere, vol. 215, by Huy, T. H.; Bui, D. P.; Kang, F.; Wang, Y. F.; Liu, S. H.; Thi, C. M.; You, S. J.; Chang, G. M.; Pham, V. V. "SnO₂/TiO₂ nanotube heterojunction: The first investigation of NO degradation by visible-light-driven photocatalysis", pages 323–332, Copyright (2018), with permission from Elsevier. This content is not subject to CC BY 4.0.

Besides the coupling with semiconductor oxides such as TiO_2 and BiOBr , recent works reported the successful combination of SnO_2 nanomaterials with conjugated polymers such as graphitic carbon nitride ($\text{g-C}_3\text{N}_4$) and polyaniline (PANI), yielding metal-free visible-light-driven photocatalysts for addressing NO gas pollution. Such combinations hold great potential because they exhibit a wide range of useful properties, including high conductivity, cost-effectiveness, high flexibility and processability, and ease of fabrication. These recent advances are highlighted and discussed in terms of preparation method and photocatalytic mechanism in this review. Regarding $\text{g-C}_3\text{N}_4$, Zou et al. successfully deposited SnO_2 quantum dots (QDs) on $\text{g-C}_3\text{N}_4$ sheets by a simple physical mixing process. The authors indicated that the $\text{SnO}_2/\text{g-C}_3\text{N}_4$ photocatalyst had a twice as high NO removal efficacy than bare SnO_2 QDs and a low NO_2 generation upon exposure to visible light for 30 min. This enhance-

ment of the photocatalytic activity was interpreted as the synergistic effect between the high photo-oxidation ability of SnO_2 triggered by the visible light response of $\text{g-C}_3\text{N}_4$. Also, the key role of the $\text{SnO}_2/\text{g-C}_3\text{N}_4$ interface in inhibiting the production of NO_2 facilitates the transition of photogenerated carriers used for the NO removal [37].

Pham et al. showcased a step-scheme (S-scheme) photocatalyst composed of 2D/0D $\text{g-C}_3\text{N}_4$ nanosheet-assisted SnO_2 NPs ($\text{g-C}_3\text{N}_4/\text{SnO}_2$) for removing NO with low NO_2 generation. This work established an S-scheme charge transfer path by combining density functional theory (DFT) calculations, trapping experiments, and electron spin resonance measurements (Figure 10). Thus, the impact of intrinsic OV within SnO_2 NPs and the resulting S-scheme heterojunction on the band structure, charge transfer, and photocatalytic activity was presented. The

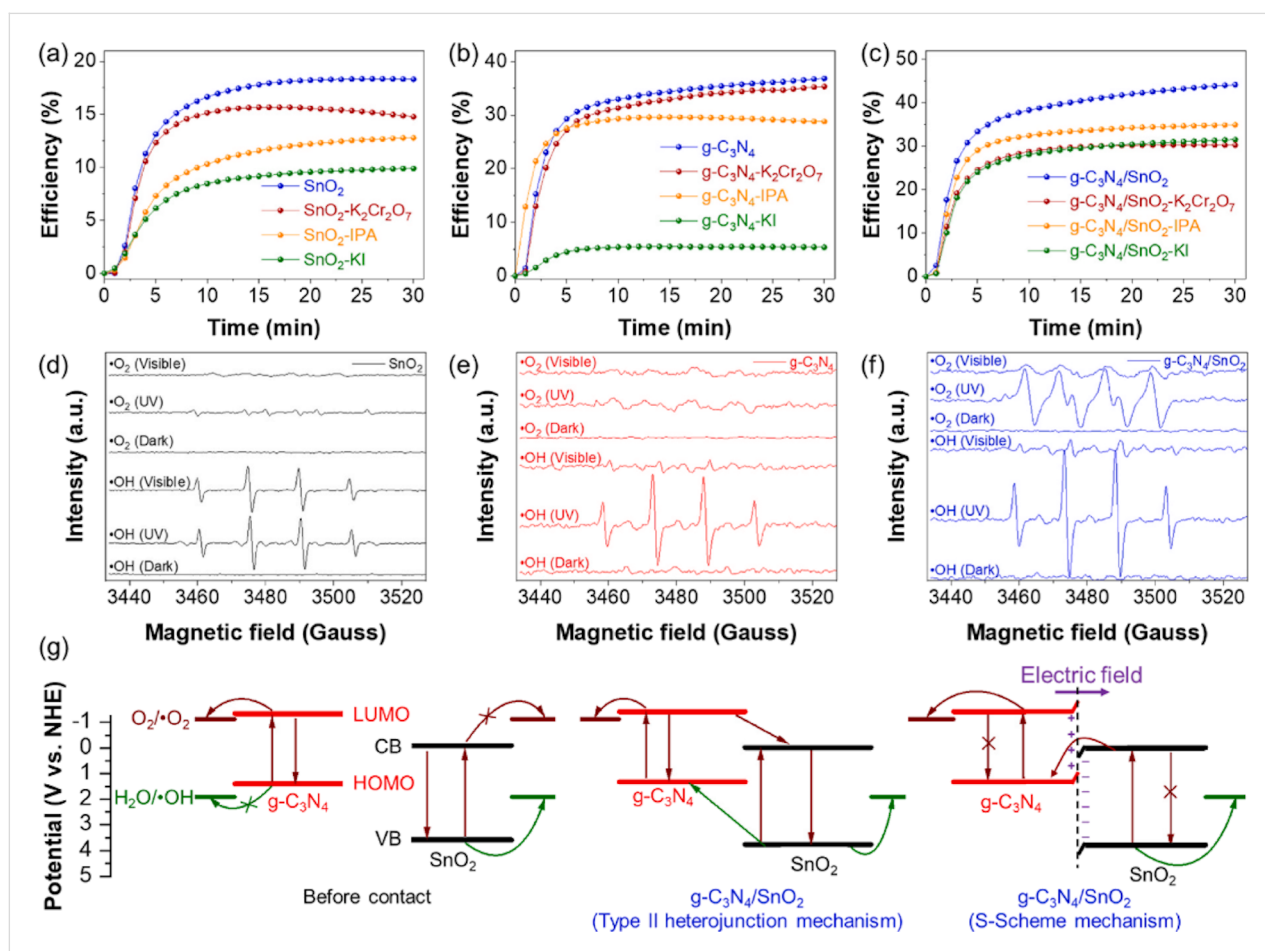


Figure 10: Photocatalytic NO removal efficacy over SnO_2 (a), $\text{g-C}_3\text{N}_4$ (b) and $\text{g-C}_3\text{N}_4/\text{SnO}_2$ (c) with scavengers under visible light ($400 < \lambda < 800$). ESR signals (d) of OH^{\cdot} radicals, and $\text{O}_2^{\cdot-}$ radicals of the materials after 10 min under visible light ($400 < \lambda < 800$). Growth curves of OH^{\cdot} radicals (e) and $\text{O}_2^{\cdot-}$ radicals (f) vs irradiation time of the materials. The charge transfer pathways of the materials (g). $\text{K}_2\text{Cr}_2\text{O}_7$, KI, and isopropyl alcohol (IPA) act as scavengers for electrons, holes, and OH^{\cdot} radicals, respectively. The brown and green arrows indicate the path of electrons and holes, respectively. Figure 10 was reprinted from [71], Environmental Pollution, vol. 286, by Van Pham, V.; Mai, D.-Q.; Bui, D.-P.; Van Man, T.; Zhu, B.; Zhang, L.; Sangkaworn, J.; Tantirungrotechai, J.; Reutrakul, V.; Cao, T. M. "Emerging 2D/0D $\text{g-C}_3\text{N}_4/\text{SnO}_2$ S-scheme photocatalyst: New generation architectural structure of heterojunctions toward visible-light-driven NO degradation", article no. 117510, Copyright (2021), with permission from Elsevier. This content is not subject to CC BY 4.0.

resulting heterojunction photocatalytically removed 40% NO (initial concentration of 500 ppb) and showed excellent photostability under visible light. The NO₂ production from the photocatalytic reaction was also negligible. The good photocatalytic NO degradation of the 2D/0D g-C₃N₄/SnO₂ catalyst is due to the defects actively trapping electrons and the charge transfer described in the S-scheme model. These factors increase the lifetime of electron–hole pairs and free radicals. The finding of this work enables the generation of a new and innovative structures with S-scheme heterojunctions for environmental treatment [71].

A similar model, a Z-scheme photocatalyst, was reported by Lu et al. who successfully fabricated a ternary nanohybrid consisting of mesoporous SnO₂, nitrogen-doped carbon quantum dots (NCDs), and ZnSn(OH)₆ using a simple in situ solvothermal method. This nanohybrid photocatalyst exhibited a

broad optical response range and excellent oxidation ability and showed great potential in addressing air pollution. The ternary Z-scheme photocatalyst could remove 37% of NO under visible light and IR without generating NO₂. In addition, this work also discussed the critical role of NCDs in extending the light harvesting range and promoting the separation of photogenerated electrons. A considerable amount of reactive oxygen radicals was produced during the photocatalytic reaction, resulting from the large amount of free surface OH groups. PL, photocurrent response, electrochemical impedance spectroscopy (EIS) data, and the nanosecond-level time-resolved fluorescence decay spectra (Figure 11) demonstrated that the SnO₂/NCDs/ZHS nanohybrid achieved low charge carrier recombination, high photoactivity, and excellent photoinduced charge transfer to the surface of the semiconductor. This study enables new insights into the underlying mechanism of heterojunction photocatalysts, especially those with Z-shaped interfaces [76].

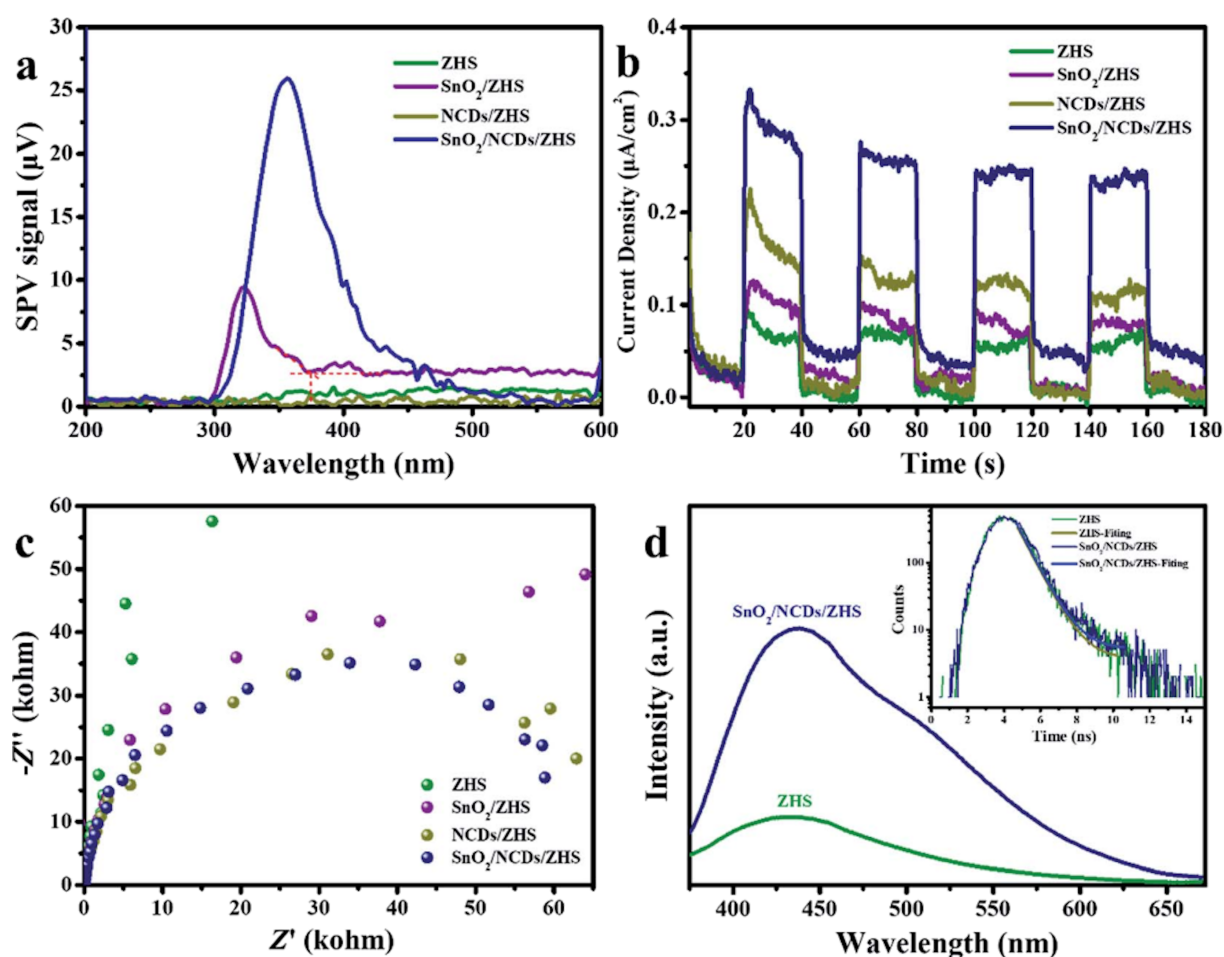


Figure 11: (a) Surface photovoltage spectroscopy, (b) transient photocurrent responses, (c) EIS Nyquist plots of ZHS, SnO₂/ZHS, NCDs/ZHS and SnO₂/NCDs/ZHS samples, and (d) PL spectra (inset: transient fluorescence decay spectra). Figure 11 was republished with permission of The Royal Society of Chemistry from [76] ("Constructing Z-scheme SnO₂/N-doped carbon quantum dots/ZnSn(OH)₆ nanohybrids with high redox ability for NO_x removal under VIS-NIR light" by Y. Lu et al., J. Mater. Chem. A, vol. 7, issue 26, © 2019); permission conveyed through Copyright Clearance Center, Inc. This content is not subject to CC BY 4.0.

Polyaniline (PANI) is a conducting polymer and compared to $g\text{-C}_3\text{N}_4$, PANI is inexpensive and easy to synthesize. Bui et al. [35] presented a SnO_2/PANI nanocomposite for photocatalytic NO removal under solar light for the first time. Furthermore, they found that the introduction of SnO_2 NPs increases the photostability of PANI during the photocatalytic process, which holds great potential for scalable manufacturing. Also, this work thoroughly discussed the adsorption and photocatalytic mechanisms, and the polymer photodegradation of the resulting nanocomposite using DFT techniques. The results confirmed that the interaction between NO and PANI is indeed a hydrogen bond and photogenerated holes serve as the primary factor of the photocatalytic NO removal [35]. Moreover, this study also indicated that hydrogen bonds between NO and PANI increased the adsorption of NO on the SnO_2/PANI surface, leading to enhanced photocatalysis. However, the photocatalytic stability of SnO_2/PANI is still a challenging problem.

Enesca et al. [29] developed photoactive heterostructures based on SnO_2 , TiO_2 , and CuInS_2 using an automated spray pyrolysis method, which is particularly beneficial for air cleaning applications. This work showed that the surface tension of the material surface directly impacts the photocatalytic activity under humid conditions. Furthermore, introducing CuInS_2 enables good UV and vis absorption thus extending the light-responsive range. As

a result, such a $\text{CuInS}_2/\text{TiO}_2/\text{SnO}_2$ heterostructure presented one of the highest photocatalytic efficacies (51.7%) in acetaldehyde removal. However, this work also opens some new questions for future studies on optimizing the band structure, which remains critical for studying charge separation [29]. In another study, a $\text{SnO}_2\text{--Zn}_2\text{SnO}_4$ Z-scheme photocatalyst system was prepared with a graphene modification to create surface vacancy sites in the composite, which contributed to an enhanced photoactivity in the oxidation of NO and acetone [75]. The presence of graphene induces the formation of SnO_2 and introduces Sn vacancies, which supports the electron transfer from the CB of Zn_2SnO_4 to oxygen under visible light irradiation (Figure 12). The authors only used a visible light LED with low power (3 W) and obtained a high efficacy of NO degradation (59.3%) [75]. However, the disadvantage of this study and other studies is that it did not determine the formation of NO_2 after the reaction (see Table 1).

Creation of narrower bandgaps

To narrow the bandgap of SnO_2 is an advanced strategy for enhancing photocatalytic ability. Specifically, reducing the bandgap of SnO_2 will increase the photoresponse in the visible light region, making up 45% of the solar spectrum. Moreover, reducing the bandgap will also create many defect states that can decrease the recombination of photogenerated electron–hole

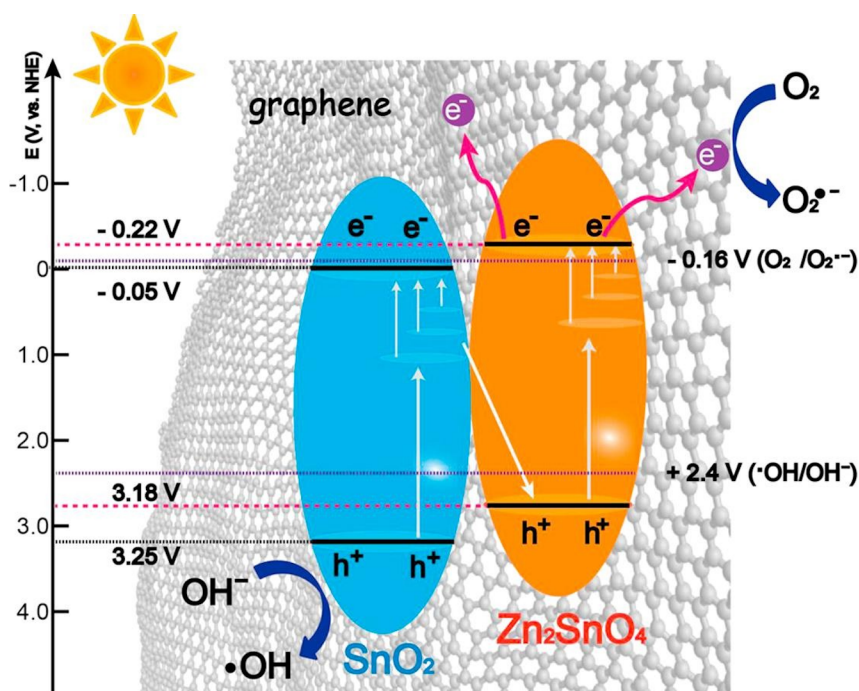


Figure 12: A mechanism of NO photocatalytic oxidation over $\text{SnO}_2\text{--Zn}_2\text{SnO}_4/\text{graphene}$. Figure 12 was reprinted from [75], Chemical Engineering Journal, vol. 336, by Li, Y.; Wu, X.; Ho, W.; Lv, K.; Li, Q.; Li, M.; Lee, S. C. "Graphene-induced formation of visible-light-responsive $\text{SnO}_2\text{--Zn}_2\text{SnO}_4$ Z-scheme photocatalyst with surface vacancy for the enhanced photoreactivity towards NO and acetone oxidation", pages 200–210, Copyright (2017), with permission from Elsevier. This content is not subject to CC BY 4.0.

pairs. There are many approaches to narrowing the bandgap of SnO_2 , such as modifying SnO_2 by noble metal, graphene, or doping, including self-doping SnO_2 (Sn^{2+} -doped SnO_2 or SnO_{2-x}). In general, doping SnO_2 will reduce the bandgap, which enhances the photoactivity in the visible light region for SnO_2 . The narrowing of the bandgap by introducing defects in metal oxide semiconductors opens up the possibility of their use in the visible spectrum [77]. Recently, Xie et al. reported using SnO_2 /graphene quantum dot (GQD) composites. They showed that the absorption edge of as-prepared SnO_2 (Figure 13a black line) is around 340 nm, equaling to a bandgap of 3.64 eV. The PL peak of SnO_2 was located in the range of 280–485 nm (Figure 13b). The combination of GQDs and SnO_2 did not affect the shape of the PL peak. However, the corresponding PL intensity of the SnO_2 /GQDs sample was decreased because of the greatly reduced radiative charge recombination of SnO_2 .

Moreover, enhanced visible light response and enhanced charge separation in the sample with GQDs have been observed (Figure 13c). The EIS measurements (Figure 13d) indicated that the diameter of the arc radius of SnO_2 /GQDs (1%) is much smaller than that of SnO_2 , confirming that the GQDs contributed to improving the charge separation, significantly reducing indoor NO under visible light irradiation. The optimized composite removed 57% of the initial NO while generating a negligible amount of NO_2 . In addition, this work found that the insertion of graphene quantum dots did not induce any noticeable impact on the structure of the SnO_2 component. Still, its presence strongly enhanced energy harvesting and charge separation in the resulting composite [36].

Regarding the self-doping SnO_2 , Pham et al. reported on the fabrication of a SnO_{2-x} /g- C_3N_4 heterojunction, inducing an

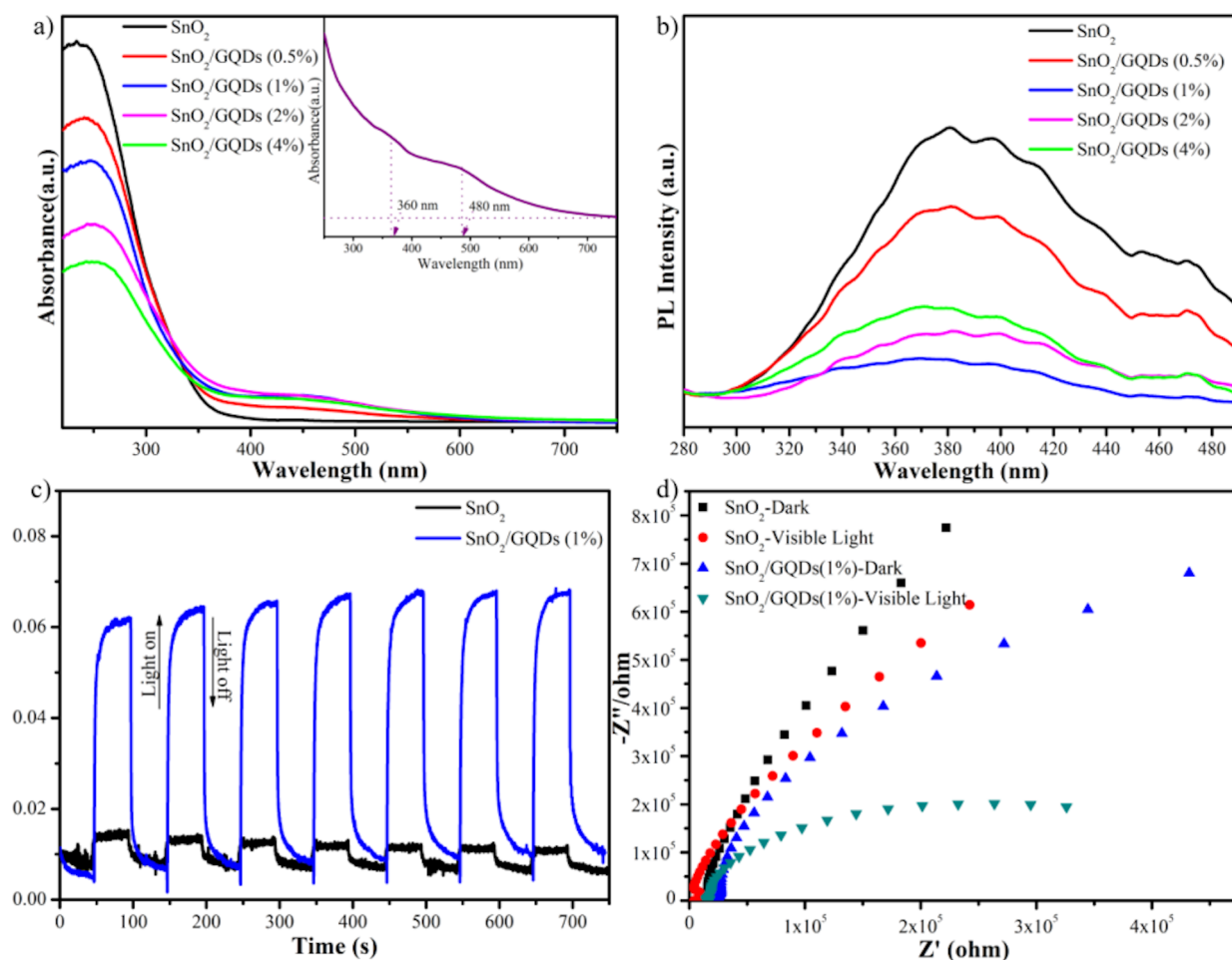


Figure 13: (a) Diffuse reflectance spectra of SnO_2 and SnO_2 /GQDs composites. Inset is the absorption spectrum of GQDs dispersed in water. (b) PL spectra of SnO_2 and SnO_2 /GQDs composites. Excitation wavelength: 260 nm. (c) Transient photocurrent response and (d) EIS curves of SnO_2 and SnO_2 /GQDs (1%) under visible light illumination and in darkness. Figure 13 was reprinted from [36], Applied Surface Science, vol. 448, by Xie, Y.; Yu, S.; Zhong, Y.; Zhang, Q.; Zhou, Y. "SnO₂/graphene quantum dots composited photocatalyst for efficient nitric oxide oxidation under visible light", pages 655–661, Copyright (2018), with permission from Elsevier. This content is not subject to CC BY 4.0.

S-scheme interface, showing impressive photocatalytic NO removal under visible light. In this work, Pham et al. indicated that deep trap centers of OV defects (Figure 14) formed with a very high concentration (36.69%), mainly from $V_{O\bullet}$ and $V_{O\bullet\bullet}$ centers. These OVs reduced the bandgaps of SnO_2 (3.7 eV) and SnO_{2-x} (3.17 eV), significantly impacting the reaction rate during the photocatalytic process, leading to enhanced NO removal under visible light. Also, the reported selectivity of the $SnO_{2-x}/g-C_3N_4$ heterojunction is three times higher than that of the bare materials. The finding of this work further supports the importance of OVs in the design of photocatalytic materials [73].

Song et al. synthesized Ce-doped SnO_2 materials with a high number of OVs to improve NO oxidation removal efficacy (Figure 15). The results showed that the excellent NO oxidation activity of Ce- SnO_2 materials was based on the OVs, which create a suitable site for the formation of NO^- intermediates to generate nitrite and nitrate products in the photocatalytic

reaction processes. Moreover, additional OVs could be readily formed by thermal treatment under argon atmosphere. The work suggested an innovative approach for developing high-performance photocatalysts and a cost-effective, environmentally benign way through heat treatment in different atmospheres [39].

Combining noble metals with SnO_2 , such as in Au/ SnO_2 [78] or Pd/ SnO_2 [79], is an advanced approach yielding an effective performance for gas sensing. However, There is only one report by Bui et al. on using Ag@ SnO_2 NPs for removing NO, taking advantage of plasmonic-induced photocatalysis [72]. The Ag@ SnO_2 NPs were fabricated by a simple and green approach using hydrothermal growth and photoreduction deposition. The introduction of Ag induced a bending of the band structure of SnO_2 NPs, leading to a change of the Fermi level. As a result, the Ag@ SnO_2 NPs showed an impressive photocatalytic NO removal of 70% while generating very little NO_2 (4%) after 30 min. In addition, this work one to understand the

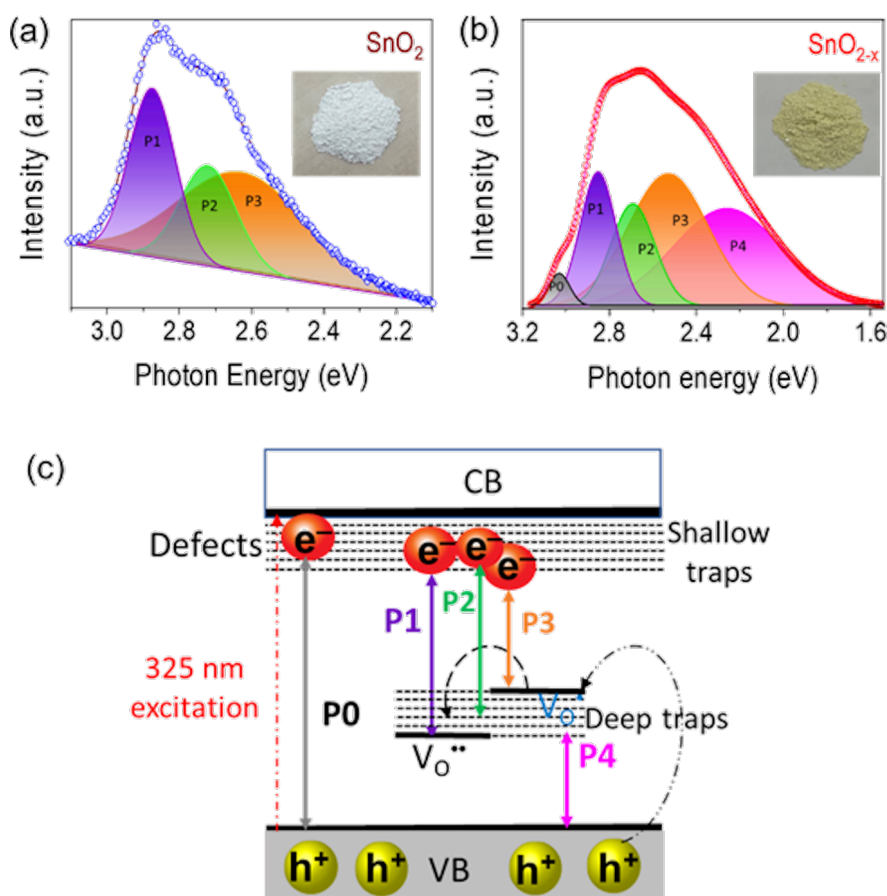
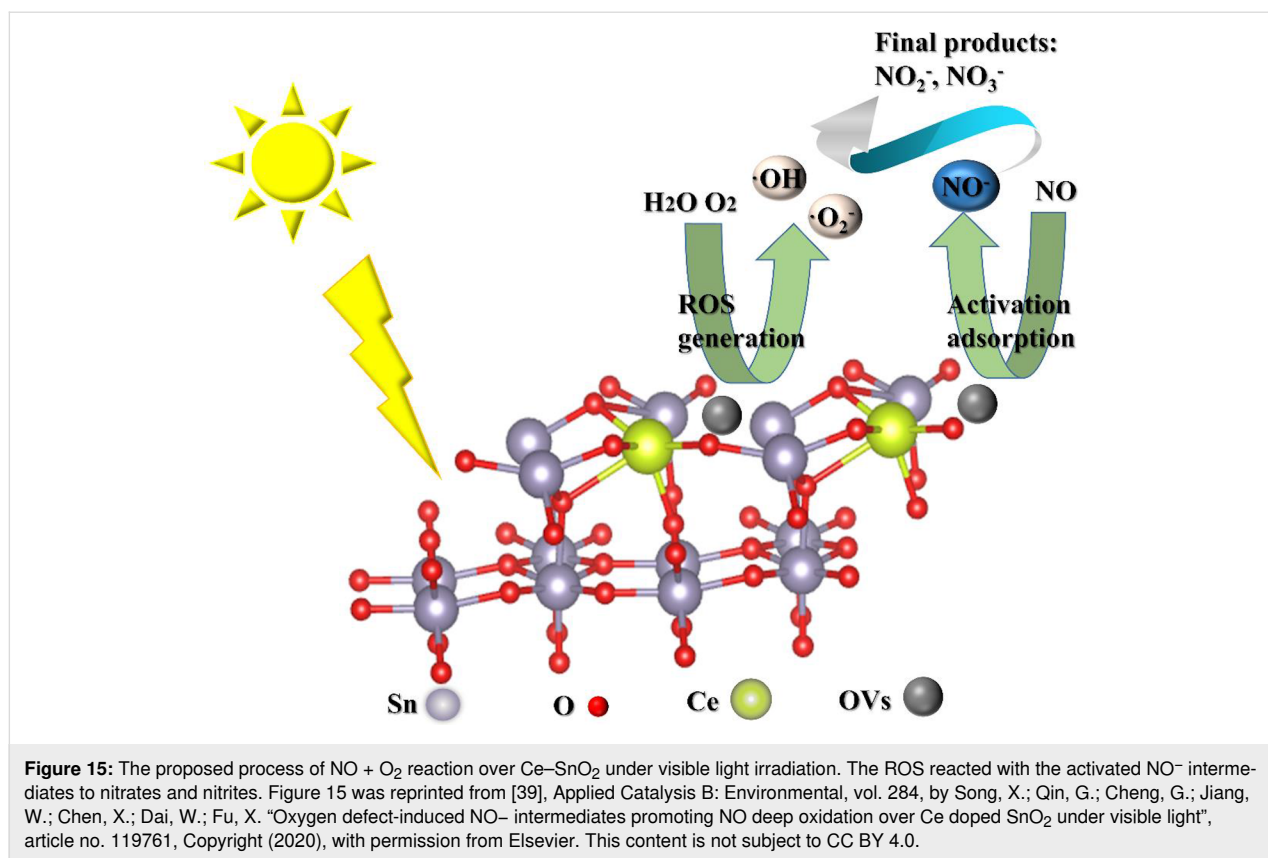


Figure 14: Gaussian fit of PL spectra with inserted images of sample color of SnO_2 (a) and SnO_{2-x} (b); and proposed schematic model for emissions from defects in SnO_2 and SnO_{2-x} (c). Figure 14 was reproduced from [73], © 2021 The Chinese Ceramic Society. Production and hosting by Elsevier B.V. This is an open access article under the CC BY-NC-ND license (<http://creativecommons.org/licenses/by-nc-nd/4.0/>). This content is not subject to CC BY 4.0.

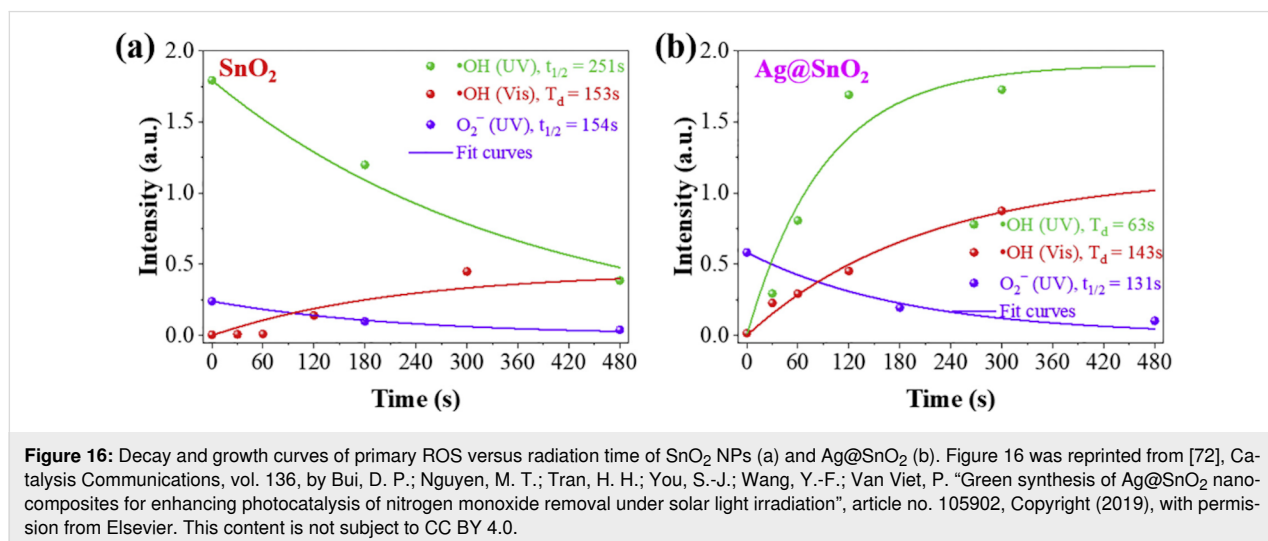


underlying photocatalytic mechanism through the species lifespan obtained from trapping experiments and time-dependent ESR signals (Figure 16). Electrons and holes are equally important for photocatalysis [72].

Conclusion

Regarding the improvement of the photocatalytic NO degradation over SnO₂ nanomaterials there are many developments and

approaches, such as BiOBr/SnO₂, g-C₃N₄/SnO₂, SnO₂/NCDs/ZnSn(OH)₆, Ce-doped SnO₂, SnO₂ self-doped with Sn²⁺, and Ag@SnO₂. These systems yielded an enhanced photocatalytic NO_x degradation either through increasing the charge transfer, through structural changes leading to bandgap reduction, or through the generation of favorable surface states for the NO_x decomposition reaction. However, the performance in NO removal is still low (only nearly 60% under visible light and



75% under solar light). Also, the syntheses of the materials are difficult to upscale to an industrial scale. Moreover, the photocatalysts were prepared in powder form, which is not suitable for emerging applications. Based on this review, we suggest the following subjects for future research: (1) improving the NO photocatalytic degradation by combining other favorable bandgap semiconductors; (2) constructing a ternary heterostructure to create double Z-scheme/S-scheme materials, preferably using two redox sites; (3) synthesizing other morphologies of SnO₂ such as nanorods, nanotubes, or 3D structures to increase the specific surface area of the catalyst; (4) upscaling the syntheses and using other synthesis approaches such as sol–gel or chemical vapor deposition to form thin film materials that can replace powder materials, (5) adhering the catalyst materials on commercial films such as polypropylene, polytetrafluorethylene, or PM2.5 films for real-life applications, such as air filters and NO_x gas treatment membranes; and (6) applying the materials in biological media where the presence of NO/NO₂ is predominant.

Acknowledgements

The authors sincerely thank the Department of Science and Technology, Ho Chi Minh City, the CM Thi Laboratory, and Mr. Sang T. Truong for support. The authors would also like to thank Elsevier, the American Chemical Society, the American Physical Society, and the Royal Society of Chemistry for allowing us to reuse some of the materials in this work.

ORCID® iDs

Viet Van Pham - <https://orcid.org/0000-0002-8697-7095>

Hong-Huy Tran - <https://orcid.org/0000-0002-7883-596X>

References

- WHO Air pollution. https://www.who.int/health-topics/air-pollution#tab=tab_1 (accessed June 23, 2021).
- WHO Regional Office for Europe. *Chapter 7.1-Nitrogen dioxide*; Copenhagen, Denmark, 2000; pp 1–33.
- United States Environmental Protection Agency. *Nitrogen Oxides Control Regulations, Ozone Control Strategies, Ground-level Ozone*; New England, 2021.
- WHO. *Ambient (outdoor) air pollution*; 2021.
- Health Canada. Residential Indoor Air Quality Guideline: Nitrogen Dioxide. 2015; <https://www.canada.ca/en/health-canada/services/publications/healthy-living/residential-indoor-air-quality-guideline-nitrogen-dioxide.html>.
- Chossiere, G. P.; Xu, H.; Dixit, Y.; Isaacs, S.; Eastham, S. D.; Allroggen, F.; Speth, R. L.; Barrett, S. R. H. *Sci. Adv.* **2021**, *7*, eabe1178. doi:10.1126/sciadv.abe1178
- United States Environmental Protection Agency. *Nitrogen Oxides (NO_x), Why and How They Are Controlled*; North Carolina, 1999.
- Haneda, M.; Ota, Y.; Doi, Y.; Hattori, M. *J. Mater. Sci.* **2016**, *51*, 10949–10959. doi:10.1007/s10853-016-0307-8
- Rajta, A.; Bhatia, R.; Setia, H.; Pathania, P. *J. Appl. Microbiol.* **2020**, *128*, 1261–1278. doi:10.1111/jam.14476
- Bogaerts, W. F.; Lampert, C. M. *J. Mater. Sci.* **1983**, *18*, 2847–2875. doi:10.1007/bf00700767
- Zou, J.; Xu, Y.; Hou, B.; Wu, D.; Sun, Y. *China Particul.* **2007**, *5*, 206–212. doi:10.1016/j.cpart.2007.03.006
- Ângelo, J.; Andrade, L.; Madeira, L. M.; Mendes, A. *J. Environ. Manage.* **2013**, *129*, 522–539. doi:10.1016/j.jenvman.2013.08.006
- Batzill, M.; Diebold, U. *Prog. Surf. Sci.* **2005**, *79*, 47–154. doi:10.1016/j.progsurf.2005.09.002
- He, Z.; Zhou, J. *Mod. Res. Catal.* **2013**, *02*, 13–18. doi:10.4236/mrc.2013.23a003
- Savioli, J.; Gavin, A. L.; Lucid, A. K.; Watson, G. W. The structure and electronic structure of tin oxides. In *Tin Oxide Materials*; Orlandi, M. O., Ed.; 2020; pp 11–39. doi:10.1016/b978-0-12-815924-8.00002-5
- Grządziel, L.; Krzywiecki, M. *Front. Nanosci.* **2019**, *14*, 215–256. doi:10.1016/b978-0-08-102572-7.00008-8
- Subramanian, V.; Burke, W. W.; Zhu, H.; Wei, B. *J. Phys. Chem. C* **2008**, *112*, 4550–4556. doi:10.1021/jp711551p
- Xiao, L.; Shen, H.; von Hagen, R.; Pan, J.; Belkoura, L.; Mathur, S. *Chem. Commun.* **2010**, *46*, 6509–6511. doi:10.1039/c0cc01156h
- Kar, A.; Kundu, S.; Patra, A. *J. Phys. Chem. C* **2011**, *115*, 118–124. doi:10.1021/jp110313b
- Birkel, A.; Lee, Y.-G.; Koll, D.; Meerbeek, X. V.; Frank, S.; Choi, M. J.; Kang, Y. S.; Char, K.; Tremel, W. *Energy Environ. Sci.* **2012**, *5*, 5392–5400. doi:10.1039/c1ee02115j
- Priya, S.; Halder, J.; Mandal, D.; Chowdhury, A.; Singh, T.; Chandra, A. *J. Mater. Sci.* **2021**, *56*, 9883–9893. doi:10.1007/s10853-021-05942-x
- Wang, Z.; Zhi, M.; Xu, M.; Guo, C.; Man, Z.; Zhang, Z.; Li, Q.; Lv, Y.; Zhao, W.; Yan, J.; Zhai, C. *J. Mater. Sci.* **2021**, *56*, 7348–7356. doi:10.1007/s10853-020-05737-6
- Jiang, S.; Yue, W.; Gao, Z.; Ren, Y.; Ma, H.; Zhao, X.; Liu, Y.; Yang, X. *J. Mater. Sci.* **2013**, *48*, 3870–3876. doi:10.1007/s10853-013-7189-9
- Li, T.-T.; Xia, L.; Yu, H.; Huang, X.-X. *J. Mater. Sci.* **2020**, *55*, 11949–11958. doi:10.1007/s10853-020-04892-0
- Anandan, K.; Rajendran, V. *Superlattices Microstruct.* **2015**, *85*, 185–197. doi:10.1016/j.spmi.2015.05.031
- Bouras, K.; Rehspringer, J.-L.; Schmerber, G.; Rinnert, H.; Colis, S.; Ferblantier, G.; Balestrieri, M.; Ihiawakrim, D.; Dinia, A.; Slaoui, A. *J. Mater. Chem. C* **2014**, *2*, 8235–8243. doi:10.1039/c4tc01202j
- Yadav, B. C.; Verma, N.; Shukla, T.; Singh, S.; Sabhajeet, S. R. *J. Mater. Sci.: Mater. Electron.* **2016**, *27*, 7852–7863. doi:10.1007/s10854-016-4776-y
- Malik, R.; Tomer, V. K.; Chaudhary, V.; Dahiya, M. S.; Rana, P. S.; Nehra, S. P.; Duhan, S. *ChemistrySelect* **2016**, *1*, 3247–3258. doi:10.1002/slct.201600634
- Enesca, A.; Yamaguchi, Y.; Terashima, C.; Fujishima, A.; Nakata, K.; Duta, A. *J. Catal.* **2017**, *350*, 174–181. doi:10.1016/j.jcat.2017.02.015
- Fan, C.; Song, X.; Yin, Z.; Yu, H.; Sun, S. *J. Mater. Sci.* **2006**, *41*, 5696–5698. doi:10.1007/s10853-006-0067-y
- Li, D.; Huang, J.; Li, R.; Chen, P.; Chen, D.; Cai, M.; Liu, H.; Feng, Y.; Lv, W.; Liu, G. *J. Hazard. Mater.* **2021**, *401*, 123257. doi:10.1016/j.jhazmat.2020.123257
- Dawar, A. L.; Kumar, A.; Sharma, S.; Tripathi, K. N.; Mathur, P. C. *J. Mater. Sci.* **1993**, *28*, 639–644. doi:10.1007/bf01151238
- Kim, S. P.; Choi, M. Y.; Choi, H. C. *Mater. Res. Bull.* **2016**, *74*, 85–89. doi:10.1016/j.materresbull.2015.10.024
- Al-Hamdi, A. M.; Rinner, U.; Sillanpää, M. *Process Saf. Environ. Prot.* **2017**, *107*, 190–205. doi:10.1016/j.psep.2017.01.022

35. Bui, P. D.; Tran, H. H.; Kang, F.; Wang, Y.-F.; Cao, T. M.; You, S.-J.; Vu, N. H.; Pham, V. V. *ACS Appl. Nano Mater.* **2018**, *1*, 5786–5794. doi:10.1021/acsanm.8b01445
36. Xie, Y.; Yu, S.; Zhong, Y.; Zhang, Q.; Zhou, Y. *Appl. Surf. Sci.* **2018**, *448*, 655–661. doi:10.1016/j.apsusc.2018.04.145
37. Zou, Y.; Xie, Y.; Yu, S.; Chen, L.; Cui, W.; Dong, F.; Zhou, Y. *Appl. Surf. Sci.* **2019**, *496*, 143630. doi:10.1016/j.apsusc.2019.143630
38. Huy, T. H.; Bui, D. P.; Kang, F.; Wang, Y.-F.; Liu, S.-H.; Thi, C. M.; You, S.-J.; Chang, G.-M.; Pham, V. V. *Chemosphere* **2019**, *215*, 323–332. doi:10.1016/j.chemosphere.2018.10.033
39. Song, X.; Qin, G.; Cheng, G.; Jiang, W.; Chen, X.; Dai, W.; Fu, X. *Appl. Catal., B* **2021**, *284*, 119761. doi:10.1016/j.apcatb.2020.119761
40. Islam, M. H.; Hogarth, C. A.; Lott, K. A. *J. Mater. Sci.* **1989**, *24*, 1305–1308. doi:10.1007/pl00020212
41. Dou, M.; Persson, C. *J. Appl. Phys.* **2013**, *113*, 083703. doi:10.1063/1.4793273
42. Zhou, W.; Liu, Y.; Yang, Y.; Wu, P. *J. Phys. Chem. C* **2014**, *118*, 6448–6453. doi:10.1021/jp500546r
43. Yu, H.; Wang, S.; Xiao, C.; Xiao, B.; Wang, P.; Li, Z.; Zhang, M. *CrystEngComm* **2015**, *17*, 4316–4324. doi:10.1039/c5ce00448a
44. Entradas, T.; Cabrita, J. F.; Dalui, S.; Nunes, M. R.; Monteiro, O. C.; Silvestre, A. J. *Mater. Chem. Phys.* **2014**, *147*, 563–571. doi:10.1016/j.matchemphys.2014.05.032
45. Mounkachi, O.; Salmani, E.; Lakhal, M.; Ez-Zahraoui, H.; Hamedoun, M.; Benaissa, M.; Kara, A.; Ennaoui, A.; Benyoussef, A. *Sol. Energy Mater. Sol. Cells* **2016**, *148*, 34–38. doi:10.1016/j.solmat.2015.09.062
46. Babu, B.; Neelakanta Reddy, I.; Yoo, K.; Kim, D.; Shim, J. *Mater. Lett.* **2018**, *221*, 211–215. doi:10.1016/j.matlet.2018.03.107
47. Fan, C.-M.; Peng, Y.; Zhu, Q.; Lin, L.; Wang, R.-X.; Xu, A.-W. *J. Phys. Chem. C* **2013**, *117*, 24157–24166. doi:10.1021/jp407296f
48. Batzill, M.; Katsiev, K.; Burst, J. M.; Diebold, U.; Chaka, A. M.; Delley, B. *Phys. Rev. B* **2005**, *72*, 165414. doi:10.1103/physrevb.72.165414
49. Van Viet, P.; Huy, T. H.; Sang, N. X.; Thi, C. M.; Van Hieu, L. *J. Mater. Sci.* **2018**, *53*, 3364–3374. doi:10.1007/s10853-017-1762-6
50. Van Viet, P.; Thi, C. M.; Hieu, L. V. *J. Nanomater.* **2016**, *2016*, 1–8. doi:10.1155/2016/4231046
51. Nam, V. H.; Van Viet, P.; Van Hieu, L.; Thi, C. M. *Mater. Res. Express* **2016**, *3*, 105901. doi:10.1088/2053-1591/3/10/105901
52. Zhong, Y.; Li, W.; Zhao, X.; Jiang, X.; Lin, S.; Zhen, Z.; Chen, W.; Xie, D.; Zhu, H. *ACS Appl. Mater. Interfaces* **2019**, *11*, 13441–13449. doi:10.1021/acsami.9b01737
53. Mäki-Jaskari, M. A.; Rantala, T. T.; Golovanov, V. V. *Surf. Sci.* **2005**, *577*, 127–138. doi:10.1016/j.susc.2005.01.004
54. Xu, G.; Zhang, L.; He, C.; Ma, D.; Lu, Z. *Sens. Actuators, B* **2015**, *221*, 717–722. doi:10.1016/j.snb.2015.06.143
55. Tiya-Djowe, A.; Dourges, M.-A.; Deleuze, H. *J. Mater. Sci.* **2020**, *55*, 4792–4807. doi:10.1007/s10853-019-04335-5
56. Wang, M.; Gao, Y.; Dai, L.; Cao, C.; Guo, X. *J. Solid State Chem.* **2012**, *189*, 49–56. doi:10.1016/j.jssc.2012.01.021
57. Jain, K.; Shrivastava, A.; Rashmi, R. *ECS Trans.* **2006**, *1* (21), 1–7. doi:10.1149/1.2218985
58. Zhao, Q.; Ju, D.; Deng, X.; Huang, J.; Cao, B.; Xu, X. *Sci. Rep.* **2015**, *5*, 7874. doi:10.1038/srep07874
59. Talebian, N.; Jafarinezhad, F. *Ceram. Int.* **2013**, *39*, 8311–8317. doi:10.1016/j.ceramint.2013.03.101
60. Park, M.-S.; Kang, Y.-M.; Wang, G.-X.; Dou, S.-X.; Liu, H.-K. *Adv. Funct. Mater.* **2008**, *18*, 455–461. doi:10.1002/adfm.200700407
61. Nahiriak, S.; Dontsova, T.; Dusheiko, M.; Smertenko, P.; Kwapinski, W. *J. Mater. Sci.: Mater. Electron.* **2020**, *31*, 21934–21947. doi:10.1007/s10854-020-04697-6
62. Matysiak, W.; Tański, T.; Smok, W.; Polishchuk, O. *Sci. Rep.* **2020**, *10*, 14802. doi:10.1038/s41598-020-71383-2
63. Shen, Y.; Wang, W.; Fan, A.; Wei, D.; Liu, W.; Han, C.; Shen, Y.; Meng, D.; San, X. *Int. J. Hydrogen Energy* **2015**, *40*, 15773–15779. doi:10.1016/j.ijhydene.2015.09.077
64. Chu, D.; Mo, J.; Peng, Q.; Zhang, Y.; Wei, Y.; Zhuang, Z.; Li, Y. *ChemCatChem* **2011**, *3*, 371–377. doi:10.1002/cctc.201000334
65. Pijolat, C.; Riviere, B.; Kamionka, M.; Viricelle, J. P.; Breuil, P. *J. Mater. Sci.* **2003**, *38*, 4333–4346. doi:10.1023/a:1026387100072
66. Wang, Y.-F.; Lei, B.-X.; Hou, Y.-F.; Zhao, W.-X.; Liang, C.-L.; Su, C.-Y.; Kuang, D.-B. *Inorg. Chem.* **2010**, *49*, 1679–1686. doi:10.1021/ic902092e
67. Le, T. H.; Truong, Q. D.; Kimura, T.; Li, H.; Guo, C.; Yin, S.; Sato, T.; Ling, Y.-C. *Solid State Sci.* **2013**, *15*, 29–35. doi:10.1016/j.solidstatesciences.2012.09.004
68. Zhang, L.; Tong, R.; Shirsath, S. E.; Yang, Y.; Dong, G. *J. Mater. Chem. A* **2021**, *9*, 5000–5006. doi:10.1039/d0ta12101k
69. Huy, T. H.; Phat, B. D.; Thi, C. M.; Van Viet, P. *Environ. Chem. Lett.* **2019**, *17*, 527–531. doi:10.1007/s10311-018-0801-0
70. Wu, H.; Yuan, C.; Chen, R.; Wang, J.; Dong, F.; Li, J.; Sun, Y. *ACS Appl. Mater. Interfaces* **2020**, *12*, 43741–43749. doi:10.1021/acsami.0c12628
71. Van Pham, V.; Mai, D.-Q.; Bui, D.-P.; Van Man, T.; Zhu, B.; Zhang, L.; Sangkaworn, J.; Tantirungrotechai, J.; Reutrakul, V.; Cao, T. M. *Environ. Pollut.* **2021**, *286*, 117510. doi:10.1016/j.envpol.2021.117510
72. Bui, D. P.; Nguyen, M. T.; Tran, H. H.; You, S.-J.; Wang, Y.-F.; Van Viet, P. *Catal. Commun.* **2020**, *136*, 105902. doi:10.1016/j.catcom.2019.105902
73. Van Viet, P.; Nguyen, T.-D.; Bui, D.-P.; Thi, C. M. *J. Materiomics* **2022**, *8*, 1–8. doi:10.1016/j.jmat.2021.06.006
74. Zhang, T.; Xu, J.; Qian, J.; Zhang, J. *J. Mater. Sci.* **2020**, *55*, 13605–13617. doi:10.1007/s10853-020-04998-5
75. Li, Y.; Wu, X.; Ho, W.; Lv, K.; Li, Q.; Li, M.; Lee, S. C. *Chem. Eng. J.* **2018**, *336*, 200–210. doi:10.1016/j.cej.2017.11.045
76. Lu, Y.; Huang, Y.; Cao, J.-j.; Li, H.; Ho, W.; Lee, S. C. *J. Mater. Chem. A* **2019**, *7*, 15782–15793. doi:10.1039/c9ta03504d
77. Kamble, V. B.; Umarji, A. M. *AIP Adv.* **2013**, *3*, 082120. doi:10.1063/1.4819451
78. Manjula, P.; Arunkumar, S.; Manorama, S. V. *Sens. Actuators, B* **2011**, *152*, 168–175. doi:10.1016/j.snb.2010.11.059
79. Zhang, K.; Yang, X.; Wang, Y.; Bing, Y.; Qiao, L.; Liang, Z.; Yu, S.; Zeng, Y.; Zheng, W. *Sens. Actuators, B* **2017**, *243*, 465–474. doi:10.1016/j.snb.2016.11.153

License and Terms

This is an open access article licensed under the terms of the Beilstein-Institut Open Access License Agreement (<https://www.beilstein-journals.org/bjnano/terms>), which is identical to the Creative Commons Attribution 4.0 International License

(<https://creativecommons.org/licenses/by/4.0>). The reuse of material under this license requires that the author(s), source and license are credited. Third-party material in this article could be subject to other licenses (typically indicated in the credit line), and in this case, users are required to obtain permission from the license holder to reuse the material.

The definitive version of this article is the electronic one which can be found at:

<https://doi.org/10.3762/bjnano.13.7>